Orbital angular momentum transfer in molecular magnets

Mahboubeh Mahdavi and Zahra Amini Sabegh
Department of Physics, University of Zanjan, University Boulevard, 45371-38791 Zanjan, Iran

Hamid R. Hamedi [*]
Institute of Theoretical Physics and Astronomy, Vilnius University, Saulėtekio 3, Vilnius LT-10257, Lithuania

Mohammad Mahmoudi [†]
Department of Physics, University of Zanjan, University Boulevard, 45371-38791 Zanjan, Iran

(Received 12 April 2021; revised 3 August 2021; accepted 9 September 2021; published 27 September 2021)

We study the propagation of probe pulses carrying orbital angular momentum (OAM) in a crystal of molecular magnets characterized by a double-Λ light-matter coupling scheme. The model is based on the four-wave mixing (FWM) of applied fields interacting with the magnetic dipole moment of the molecular magnets. We consider the light-matter interaction under the situation where a weak probe field carries an optical vortex and investigate the exchange of optical vortices between different frequencies via the FWM in the microwave region. The propagation of OAM beams with nonzero radial indices is then explored. It is found that the conservation of both azimuthal and radial indices is satisfied over the swapping of OAM states of light. Superimposing two initially weak OAM modes with different topological charges creates specific vortex beams with a very characteristic form. The resulting beam contains a central vortex as well as several singly charged peripheral vortices distributed at the same radial distance from the center of the light beam. This complex pattern of vortices arises because the intensity radius of two interfering OAM modes is different. It is shown that the boundary region of intensity dominance of two OAM modes can be controlled by the molecular magnets parameters and strong cw electromagnetic fields. Our proposed scheme may provide a route to study the solid systems suitable for quantum technologies as well as for OAM exchange devices for quantum information processing.

DOI: 10.1103/PhysRevB.104.094432

I. INTRODUCTION

Single-molecule magnets (SMMs) are nanoscale molecules, composed of magnetic metals surrounded by nonmagnetic atoms (ligands) [1]. The size of SMMs changes from 1 to 100 nm depending on the composition of the ligands. Owing to the existence of ligands, the interaction between different molecules in the crystal lattice is less than that of the intramolecular interactions. The system can then be considered as noninteracting SMMs. Compared to a free electron, they demonstrate many spin eigenstates with a potential-energy barrier that separates opposite spin projections. Due to their molecular nature, SMMs can exhibit a variety of quantum effects, including quantum tunneling of magnetization and quantum steps in the macroscopic properties of the system [1–3]. SMMs combine the classical macroscale and quantum nanoscale properties [4]. These types of molecules provide a powerful source of coherent microwave radiation [5] and allow scientists for further advances in quantum computing [6], storage and information processing [7], and various spintronics devices [8], all of which are made possible through their long magnetic relaxation times at low temperatures and nanoscale size. In addition, the interaction between molecular magnets and the electromagnetic waves or acoustic waves leads to fascinating and novel optical phenomena, such as electromagnetically induced transparency (EIT) [9], four-wave mixing via EIT [10], ultraslow microwave solitons [11], nonlinear propagation of acoustic wave via EIT [12], and parametric interaction of two acoustic waves in the presence of a strong ac magnetic field [13].

On the other hand, optical vortices, also known as orbital angular momentum (OAM) beams, have been widely studied in classical and quantum optics. An optical vortex has the features of transverse field distribution with an azimuthal angular dependence of the form $\exp(il\varphi)$, where φ is the azimuthal angle and l is the topological charge (or azimuthal index) which could be either positive or negative corresponding to the rotation of the screw wave front [14]. These beams have a doughnut-shaped pattern since the phase is undeterminable at the dark center of the wave packet. The azimuthal component of the beams' Poynting vector makes a helical flow of energy around the optical axis. Various applications are found for vortex beams, e.g., in optical communication [15,16], optical tweezers [17], and quantum information [18]. The creation of optical vortices has attracted much attention in high wavelength ranges, such as microwaves, which are widely used in radar imaging [19,20], target detection [21], manipulation of

[*]hamid.hamedi@tfai.vu.lt
[†]mahmoudi@znu.ac.ir

macroscopic objects [22], and data transmission [23]. Several methods have been proposed for the generation of optical vortices in microwave frequency including spiral phase plates [24], circular traveling-wave antenna [25], dielectric resonator antenna [26], substrate integrated cavity resonator antenna [27], and planar metasurface [28]. It should be noted that the spiral phase plates method is not suitable because of difficulties in the precise fabrication of spiral phase plates. Moreover, it can only generate the single-mode OAM beams under a large angle of divergence. An OAM beam may have relatively low output gain [29] in methods based on the antenna. However, in contrast to the conventional approaches, nonlinear processes permit an efficient generation of microwave optical vortices in different frequencies. Also, in a crystal of molecular magnets, varying the intensity of the dc magnetic field is a simple method for adjusting the frequency of the generated optical vortices. Various methods have been reported to investigate the intensity and phase structure of the final optical vortices including two-beam interference technique [30] and diffraction patterns [31–33]. Recently, an experimental scheme based on the weak measurement principle has been proposed for measuring the OAM [34].

The frequency conversion processes in which one or two beams with different frequencies give rise to a nonlinear material polarization term are very useful in generating an optical vortex with a higher wavelength. Numerous papers have explored the propagation of optical vortices in nonlinear media via different mechanisms, such as the second-harmonic generation [35,36], the four-wave mixing (FWM) [37–40], the sum-frequency generation [41], and the spatially structured EIT [42,43]. The recently proposed and demonstrated proposals for the exchange of optical vortices in matter waves have emerged as a direct connection to the OAM-based applications [44–49]. In this context, the exchange of OAM modes in four- and five-level quantum systems has been explored by Ruseckas *et al.* [50], Ruseckas *et al.* [51], Hamedi *et al.* [52], Hamedi *et al.* [53], and Hamedi *et al.* [54]. Transfer of OAM in structural asymmetry quantum-dot molecules has been recently shown to be possible via the effect of interdot tunneling [55]. Yet, the generated beam falls in the range of visible wavelengths.

In this paper, we study the exchange of optical vortices in a crystal of molecular magnets via the FWM mechanism in the presence of a dc magnetic field and four electromagnetic waves. We show that a single probe beam carrying an OAM initially shined on one transition of the four-level molecule magnets creates a new probe pulse with the same azimuthal and radial indices as that of the incident beam. Interfering two initially nonzero vortices are found to produce a pattern of complex beams with peripheral vortices propagating inside the molecular magnets crystal. It is the shear in the phase of two initial vortices positioned at different radii that generates such composite off-axis singularity beams. Note that, although both schemes proposed here and in Ref. [53] are based on a double-Λ light-matter coupling, there exist differences between them. It is an atomic system in Ref. [53] that interacts with optical vortices, whereas the double-Λ coupling scheme proposed here is formed in molecular magnets. On the other hand, the electric-field components of the laser fields in Ref. [53] interplay with an atomic system, whereas the magnetic-field components of the electromagnetic waves interact here with molecular magnets due to their large ground-state spin. The results presented here might be much more practical than that of the atomic system because of the flexible design and the large ground-states spin coherence of the host medium [7].

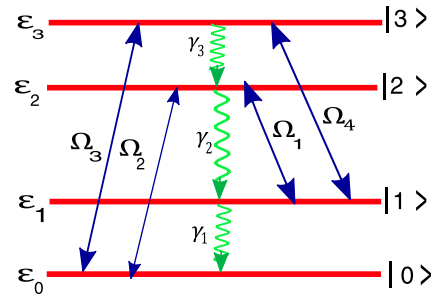

FIG. 1. Four-level system of one single molecular magnet.

II. THEORETICAL FRAMEWORK

Let us consider a system of SMMs in the presence of a dc magnetic-field H_0 (perpendicular to the easy anisotropy axis of the molecules) which can tune the energy transition frequency in the range of microwave (Fig. 1). Electromagnetic waves with their magnetic fields interact with the SMMs under the condition of low temperatures. As a realistic example, we consider an Mn_{12} acetate molecule made of 12 manganese included in eight Mn^{3+} ions with (spin $S = 2$) and four Mn^{4+} ions with ($S = 3/2$). Magnetically coupling of these ions yields the creation of the ground-state $S = 10$ [56]. The spin ground state consists of $2S + 1$ degenerate levels with different m_s's, $-S \leqslant m_s \leqslant S$. In a real experiment, the SMM crystals are included 10^{10}–10^{15} independent single-crystal units of up to 10–100 μm in length. Therefore, the SMMs can be considered as a single spin and described by the Hamiltonian of the single spin [6]. We have considered the four lowest-energy levels of $2S + 1$ spin states as $|0\rangle$, $|1\rangle$, $|2\rangle$, and $|3\rangle$. We assume z and x axes along the easy anisotropy axis and dc magnetic field, respectively. So the eigenstates $|0\rangle$ and $|2\rangle$ should be symmetric whereas $|1\rangle$ and $|3\rangle$ are antisymmetric. Therefore, the spin matrix elements, considering the selection rules for the symmetric feature of corresponding eigenstates, are given by

$$\begin{aligned}
&\langle 2|\hat{S}_x|0\rangle \neq 0, \quad \langle 2|\hat{S}_y|0\rangle = \langle 2|\hat{S}_z|0\rangle = 0,\\
&\langle 3|\hat{S}_x|1\rangle \neq 0, \quad \langle 3|\hat{S}_y|1\rangle = \langle 3|\hat{S}_z|1\rangle = 0,\\
&\langle 2|\hat{S}_x|1\rangle = 0, \quad \langle 2|\hat{S}_y|1\rangle \neq 0, \quad \langle 2|\hat{S}_z|1\rangle \neq 0,\\
&\langle 3|\hat{S}_x|0\rangle = 0, \quad \langle 3|\hat{S}_y|0\rangle \neq 0, \quad \langle 3|\hat{S}_z|0\rangle \neq 0. \qquad (1)
\end{aligned}$$

The magnetic fields of the applied electromagnetic waves H_2 and H_4 (H_1 and H_3) are polarized along the $x(y)$ axes. Two strong cw electromagnetic fields with the Rabi frequencies Ω_1 and Ω_4 are applied to the $|1\rangle \leftrightarrow |2\rangle$ and $|1\rangle \leftrightarrow |3\rangle$ transitions. The transitions $|0\rangle \leftrightarrow |2\rangle$ and $|0\rangle \leftrightarrow |3\rangle$ are also excited by two weak electromagnetic fields with Rabi frequencies Ω_2 (probe field) and Ω_3 (FWM-generated field), respectively.

The magnetic properties are described using a spin Hamiltonian for one molecule, which can be written as $\hat{H} = \hat{H}_0 + \hat{V}$ with ($\hbar = 1$) [9],

$$\hat{H}_0 = -D\hat{S}_z^{\,2} + \hat{H}_{tr} - g\mu_B\hat{S}_x H_0,$$
$$\hat{V} = -\frac{g\mu_B}{2}\sum_{j=1}^{4}\hat{\mathbf{S}}\cdot H_j e^{-i\omega_j t + ik_j r} + \text{H.c.} \qquad (2)$$

The first term in the Hamiltonian $\hat{H}_0$ represents the uniaxial anisotropy resulting from the spin-orbit coupling (SOC) and generates an energy barrier DS_z^2 separating opposite spin projections. The second term stands for the transverse anisotropy $\hat{H}_{tr}$ which has a crucial role in the tunneling effect and interference of the states in the SMMs [57]. It is worth noting that the transverse anisotropy is negligible with respect to the longitudinal one in the Mn_{12} acetate and has been dropped [9]. The SOC, including the longitudinal and transverse anisotropy, mixes the energy states leading to the correlation between them [58]. The longitudinal anisotropy in the spin Hamiltonian destroys the degeneracy of the spin states and decreases the correlation. However, the transverse anisotropy, responsible for the quantum tunneling between the states, plays a crucial role in increasing the correlation. Since we can ignore the transverse anisotropy in comparison to the longitudinal one in the Mn_{12} acetate SMM crystal, the correlation has no considerable effect on the intended transitions. The term $-g\mu_B\hat{S}_x H_0$ describes the Zeeman energy associated with the interaction of the spin of the molecule with an externally applied magnetic-field H_0. Here, the longitudinal anisotropy energy constant, the Landé factor, and the Bohr magneton are denoted by D, g, and μ_B, respectively. Experimental values for the Mn_{12} acetate are $S = 10$, $D = 0.68K$, $\hat{H}_{tr} = -C(\hat{S}_+^4 + \hat{S}_-^4)$ with $C = 6\times10^{-5}$, $H_0 = 60$ kOe, and $g = 1.9$ [9]. The easy anisotropy of the molecule is considered to be along the z axis. The spin operator is defined by $\hat{\mathbf{S}}$ with $\hat{S}_x$, $\hat{S}_y$, and $\hat{S}_z$ being the projections of the spin operator along the x, y, and z axes, respectively. The operator of the interaction of the molecule with the ac fields is denoted by $\hat{V}$. The eigenstates $|n\rangle$ and eigenenergies $\varepsilon_n (n = 0\text{–}2, \ldots)$ are determined by the eigenvalue equation $\hat{H}_0|n\rangle = \varepsilon_n|n\rangle$ so that $\hat{H}_0 = \sum_n \varepsilon_n|n\rangle\langle n|$. The Hamiltonian $\hat{H}_{int}$ in the interaction picture reads

$$\begin{aligned}\hat{H}_{int} &= e^{i\hat{H}_0 t}\hat{V}e^{-i\hat{H}_0 t}\\ &= -\Omega_1 e^{-i\Delta_{21}t + i\mathbf{k_1}\cdot\mathbf{r}}|2\rangle\langle 1| - \Omega_2 e^{-i\Delta_{20}t + i\mathbf{k_2}\cdot\mathbf{r}}|2\rangle\langle 0|\\ &\quad -\Omega_3 e^{-i\Delta_{30}t + i\mathbf{k_3}\cdot\mathbf{r}}|3\rangle\langle 0| - \Omega_4 e^{-i\Delta_{31}t + i\mathbf{k_4}\cdot\mathbf{r}}|3\rangle\langle 1|, \qquad (3)\end{aligned}$$

where $\Delta_{ij} = \omega_{ij} - \overline{\omega}_{ij}$ describes the frequency detuning of the applied fields and the corresponding transitions $|i\rangle \leftrightarrow |j\rangle$. Rabi frequencies are defined as

$$\Omega_1 = \frac{g\mu_B H_1}{2\hbar}\langle 2|\hat{S}_y|1\rangle, \quad \Omega_2 = \frac{g\mu_B H_2}{2\hbar}\langle 2|\hat{S}_x|0\rangle,$$
$$\Omega_3 = \frac{g\mu_B H_3}{2\hbar}\langle 3|\hat{S}_y|0\rangle, \quad \Omega_4 = \frac{g\mu_B H_4}{2\hbar}\langle 3|\hat{S}_x|1\rangle, \qquad (4)$$

with H_j characterizing the magnitude of the magnetic field of electromagnetic waves $\mathbf{H_j}$. Note that, all matrix elements $\langle i|\hat{S}_\alpha|j\rangle$, ($\alpha = x, y$; $i, j = 0\text{–}3$) are equal to zero except $\langle 2|\hat{S}_y|1\rangle$, $\langle 2|\hat{S}_x|0\rangle$, $\langle 3|\hat{S}_y|0\rangle$, and $\langle 3|\hat{S}_x|1\rangle$ in Eq. (4). In this situation, the forbidden transitions imposed by the symmetry selection rules can be changed to the allowed transitions in the presence of the external magnetic field, laser pulse or inclusion of the SOC [59]. Using the Liouville equation, the dynamic of the medium is governed by the time-dependent density matrix equations,

$$\begin{aligned}
\dot{\rho}_{00} &= \gamma_1\rho_{11} + i\Omega_2^*\rho_{20} + i\Omega_3^*\rho_{30} - i\Omega_2\rho_{02} - i\Omega_3\rho_{03},\\
\dot{\rho}_{11} &= -\gamma_1\rho_{11} + \gamma_2\rho_{22} + i\Omega_1^*\rho_{21} + i\Omega_4^*\rho_{31} - i\Omega_1\rho_{12} - i\Omega_4\rho_{13},\\
\dot{\rho}_{22} &= -\gamma_2\rho_{22} + \gamma_3\rho_{33} + i\Omega_2\rho_{02} + i\Omega_1\rho_{12} - i\Omega_2^*\rho_{20} - i\Omega_4^*\rho_{21},\\
\dot{\rho}_{01} &= \left[i(\Delta_{21} - \Delta_{20}) - \frac{\gamma_1}{2}\right]\rho_{01} + i\Omega_2^*\rho_{21} + i\Omega_3^*\rho_{31} - i\Omega_1\rho_{02} - i\Omega_4\rho_{03},\\
\dot{\rho}_{02} &= \left[-i\Delta_{20} - \frac{\gamma_2}{2}\right]\rho_{02} + i\Omega_2^*(\rho_{22} - \rho_{00}) + i\Omega_3^*\rho_{32} - i\Omega_1^*\rho_{01},\\
\dot{\rho}_{03} &= \left[-i\Delta_{30} - \frac{\gamma_3}{2}\right]\rho_{03} + i\Omega_3^*(\rho_{33} - \rho_{00}) + i\Omega_2^*\rho_{23} - i\Omega_4^*\rho_{01},\\
\dot{\rho}_{12} &= \left[-i\Delta_{21} - \frac{\gamma_1 + \gamma_2}{2}\right]\rho_{12} + i\Omega_1^*(\rho_{22} - \rho_{11}) + i\Omega_4^*\rho_{32} - i\Omega_2^*\rho_{10},\\
\dot{\rho}_{13} &= \left[-i\Delta_{31} - \frac{\gamma_1 + \gamma_3}{2}\right]\rho_{13} + i\Omega_4^*(\rho_{33} - \rho_{11}) + i\Omega_1^*\rho_{23} - i\Omega_3^*\rho_{10},\\
\dot{\rho}_{23} &= \left[i(\Delta_{20} - \Delta_{30}) - \frac{\gamma_3 + \gamma_2}{2}\right]\rho_{23} + i\Omega_2\rho_{03} + i\Omega_1\rho_{13} - i\Omega_3^*\rho_{20} - i\Omega_4^*\rho_{21},\\
\dot{\rho}_{33} &= -(\dot{\rho}_{00} + \dot{\rho}_{11} + \dot{\rho}_{22}),
\end{aligned} \qquad (5)$$

where the decay rates for the transitions $|1\rangle \leftrightarrow |0\rangle$, $|2\rangle \leftrightarrow |1\rangle$, $|3\rangle \leftrightarrow |2\rangle$ are indicated by γ_1, γ_2, and γ_3, respectively. The decay rates have been added phenomenologically in the above density-matrix equations. It is well known that the decay rate effects contribute to the loss of coherence. Furthermore, the decoherence processes have vital importance since they dictate the direction of the population transfer in the Λ process, especially in the search for the steady-state condition [60,61]. Here, nonadjacent spontaneous emissions have no significant effect on the EIT region and have been ignored in calculations. Solving Eq. (5) for $\Delta_{21} = \Delta_{31} = \Delta_{30} = \Delta_{20} = 0$, the steady-state analytical expressions for the coherence terms ρ_{20} and ρ_{30} read

$$\rho_{20} = \frac{2i(\gamma_1\gamma_3\Omega_2 - 4\Omega_1\Omega_3\Omega_4^* + 4\Omega_2|\Omega_4|^2)}{\gamma_1\gamma_2\gamma_3 + 4\gamma_3|\Omega_1|^2 + 4\gamma_2|\Omega_4|^2},$$
$$\rho_{30} = \frac{2i(\gamma_1\gamma_2\Omega_3 + 4\Omega_1\Omega_3\Omega_1^* - 4\Omega_2\Omega_4\Omega_1^*)}{\gamma_1\gamma_2\gamma_3 + 4\gamma_3|\Omega_1|^2 + 4\gamma_2|\Omega_4|^2}. \quad (6)$$

The FWM susceptibility is proportional to the coherence term of the transition ρ_{30}. Therefore, the gain and absorption coefficients of the generated field coupled to the transition $|3\rangle \leftrightarrow |0\rangle$ depend on the imaginary part of the coherence term ρ_{30} ($\mathrm{Im}[\rho_{30}]$). In our notation, $\mathrm{Im}[\rho_{30}] < 0$ indicates amplification of the FWM-generated field whereas $\mathrm{Im}[\rho_{30}] > 0$ means absorption of the beam.

The evolution of two weak fields is described by the Maxwell equations [62],

$$\frac{-\partial^2 H}{\partial z^2} + \frac{1}{c^2}\frac{\partial^2 H}{\partial t^2} = -\frac{4\pi}{c^2}\frac{\partial^2 M}{\partial t^2}, \quad (7)$$

where c is the speed of light in the vacuum. The magnetization of field M is given by

$$\vec{M} = g\mu_B n\,\mathrm{Tr}(\hat{\rho}\hat{S}), \quad (8)$$

where n shows the number of molecules per unit volume. Using Eqs. (7) and (8), the partial differential equations for two time-independent probe fields in the slowly varying envelope approximation are described by [9]

$$\frac{\partial\Omega_2(z)}{\partial z} = i\eta_2\rho_{20},$$
$$\frac{\partial\Omega_3(z)}{\partial z} = i\eta_3\rho_{30}, \quad (9)$$

where $\eta_2 = n\pi\omega_2(g\mu_B|\langle 0|\hat{s}_x|2\rangle|)^2/\hbar\upsilon$ and $\eta_3 = n\pi\omega_3(g\mu_B|\langle 0|\hat{s}_y|3\rangle|)^2/\hbar\upsilon$. To study the propagation of fields inside the SMM crystal, we solve the differential Eqs. (9) under the boundary conditions where only the weak probe field Ω_2 is illuminated at $z = 0$. Another weak FWM field Ω_3 will be generated in the propagation axis via the FWM within the system of the molecular magnet. Substituting Eq. (6) into Eq. (9) and assuming $\gamma_1 = 0$, $\Omega_3(z = 0) = 0$, and $\Omega_2(z = 0) = \Omega_2$, one arrives at the set of equations,

$$\Omega_2(r,\varphi,z) = -\frac{\exp\left(\frac{2z}{L}\frac{(-\eta_3|\Omega_1|^2-\eta_2|\Omega_4|^2)}{\gamma_3|\Omega_1|^2+\gamma_2|\Omega_4|^2}\right)\eta_2|\Omega_4|^2\Omega_2(r,\varphi)}{\eta_3|\Omega_1|^2+\eta_2|\Omega_4|^2}$$
$$-\frac{\eta_3|\Omega_1|^2\Omega_2(r,\varphi)}{\eta_3|\Omega_1|^2+\eta_2|\Omega_4|^2}, \quad (10)$$

and

$$\Omega_3(r,\varphi,z) = -\frac{\exp\left(\frac{2z}{L}\frac{(-\eta_3|\Omega_1|^2-\eta_2|\Omega_4|^2)}{\gamma_3|\Omega_1|^2+\gamma_2|\Omega_4|^2}\right)\eta_3\Omega_2(r,\varphi)\Omega_4\Omega_1^*}{\eta_3|\Omega_1|^2+\eta_2|\Omega_4|^2}$$
$$+\frac{\eta_3\Omega_2(r,\varphi)\Omega_4\Omega_1^*}{\eta_3|\Omega_1|^2+\eta_2|\Omega_4|^2}, \quad (11)$$

which describe the propagation of fields inside the medium.

III. RESULTS AND DISCUSSIONS

The complex form describing the distribution of the field amplitude of an Laguerre-Gauss (LG) beam can be expressed in cylindrical cordinates as [63]

$$\Omega(r,\varphi) = \Omega_0\frac{1}{\sqrt{|l|!}}\left(\frac{\sqrt{2}r}{w_{LG}}\right)^{|l|}L_p^{|l|}\left(2r^2/w_{LG}^2\right)e^{-r^2/w_{LG}^2}\,e^{il\varphi}, \quad (12)$$

where Ω_0, w_{LG}, l, and p show the strength, beam waist, azimuthal (OAM) and radial indices of the LG modes, respectively. The associated Laguerre polynomial, $L_p^{|l|}$ has the form

$$L_p^{|l|}(x) = \frac{e^x x^{-|l|}}{p!}\frac{d^p}{dx^p}[x^{|l|+p}e^{-x}], \quad (13)$$

with $x = 2r^2/w_{LG}^2$ determining the radial dependence of the LG beams for different radial mode numbers. The LG light beams possess OAM along the optical axis for $l \neq 0$.

A. Exchange of optical vortices

Let us now study the evolution of both probe field intensities (related to applied and generated probe fields) in the presence of two strong cw fields. Having in mind the analytical form of both weak fields presented in Eqs. (10) and (11), the FWM-generated electromagnetic field explicitly depends on the Rabi frequency of two strong cw beams

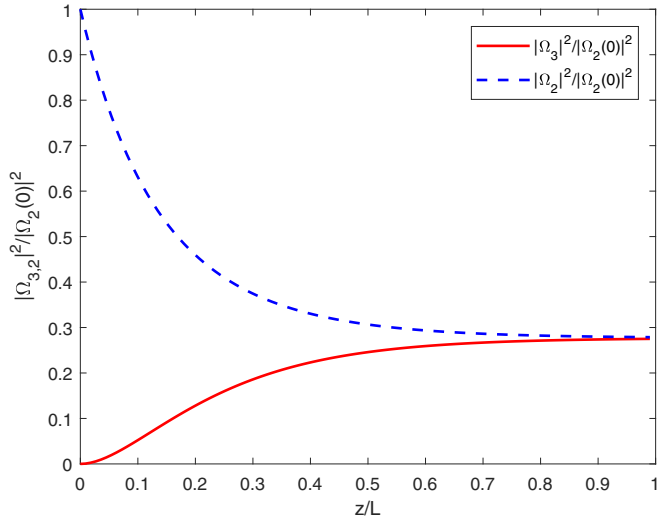

FIG. 2. The dimensionless intensity of fields $|\Omega_2(z)|^2/|\Omega_2(0)|^2$ and $|\Omega_3(z)|^2/|\Omega_2(0)|^2$ versus the dimensionless distance z/L for $\Omega_1 = 4\gamma$, $\Omega_4 = 4\gamma$, $\eta_2 = 0.9\eta_3$, $\eta_3 = 3\gamma/z$, and $\gamma_2 = \gamma_3 = \gamma$.

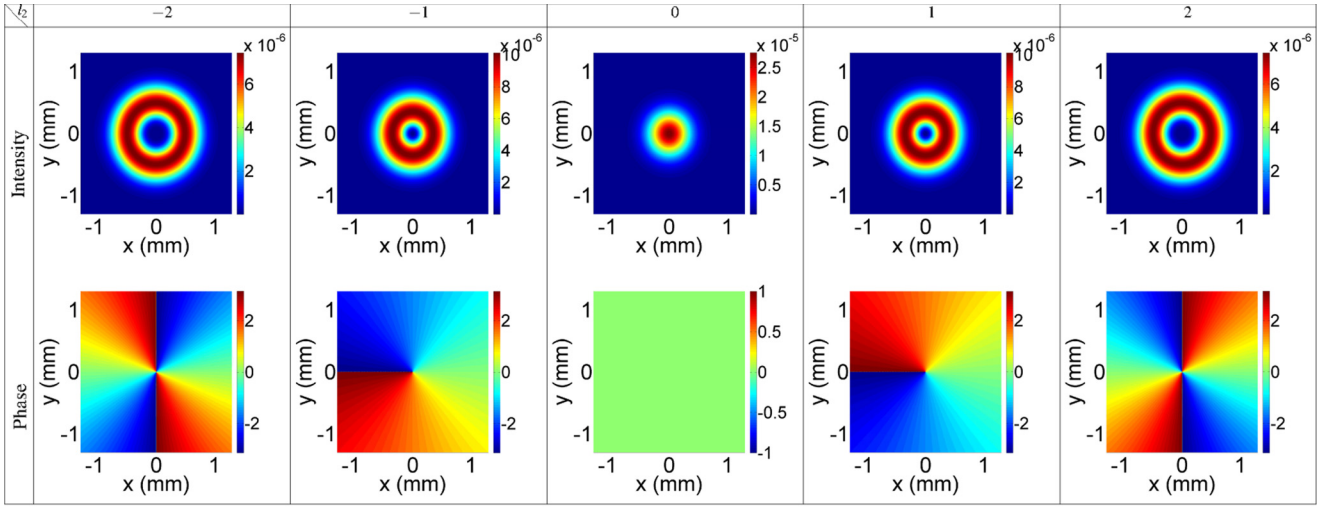

(a)

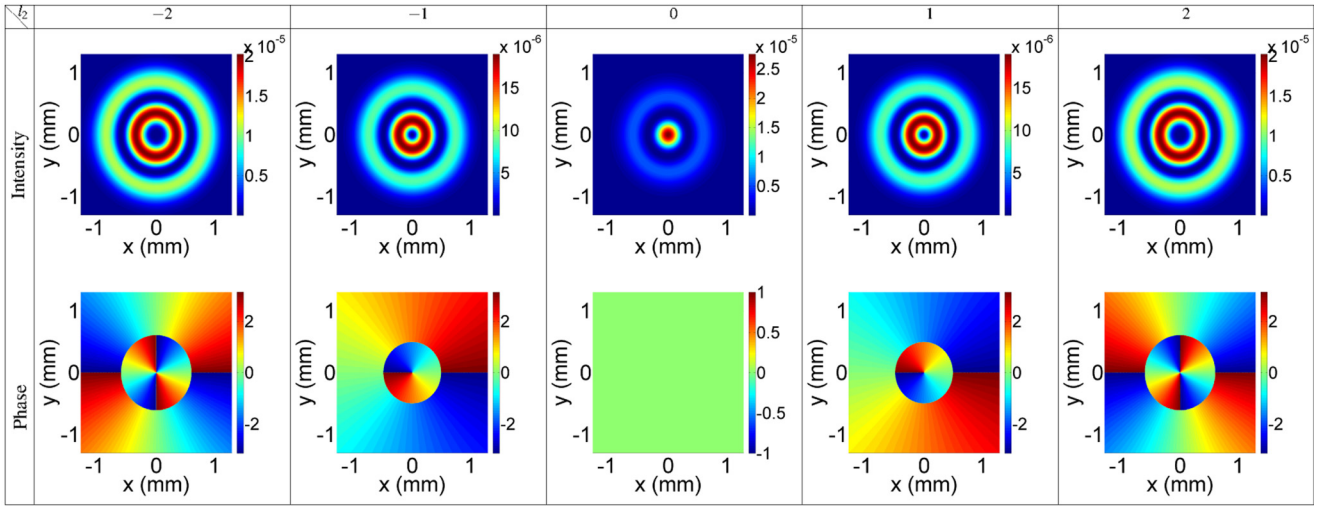

(b)

FIG. 3. The intensity and phase profiles of the FWM-generated field as a function of x and y with a zero radial index (a) $p_2 = 0$ and (b) $p_2 = 1$ for $-2 < l_2 < 2$. We take $w_{LG} = 0.5$ mm and $\Omega_{2_0} = 0.01\gamma$. Other parameters are the same as in Fig. 2.

Ω_1, Ω_4, and the weak applied pulsed probe. This indicates that the FWM-generated beam Ω_3 acquires a vortex if any of the fields Ω_2, Ω_4 are initially vortices. We assume a condition where the probe field Ω_2 is initially a vortex and displayede in Fig. 2 the dimensionless intensities $|\Omega_2(z)|^2/|\Omega_2(0)|^2$ and $|\Omega_3(z)|^2/|\Omega_2(0)|^2$ against the dimensionless distance z/L when $\eta_2 = 0.9\eta_3$, $\eta_3 = 3\gamma/z$, $\Omega_1 = 4\gamma$, $\Omega_4 = 4\gamma$, and $\gamma_2 = \gamma_3 = \gamma$. Both strong cw fields Ω_1 and Ω_4 are always on and remain unchanged with respect to the time t and coordinate z. One can see that the FWM-generated field Ω_3 has not yet been created at the beginning of the ensemble where the weak probe field Ω_2 has just entered. The FWM-generated field appears as propagating inside the molecular magnet. Equations (10) and (11) as well as Fig. 2 indicate that both OAM beams experience energy losses at the beginning of the ensemble; losses disappear going deeper where the system transfers to some transparency state. Moreover, the coupling constants, i.e., η_2 and η_3 have a strong impact on the propagation of the probe and FMW-generated fields. Note that the amplitude of the FWM-generated field is sufficiently large when $\eta_2 < \eta_3$, providing an effective energy transfer between the probe and FWM-generated fields. The azimuthal modulation of the FWM-generated field is displayed in Fig. 3 for the case that only Ω_2 is a vortex. We take $w_{LG} = 0.5$ mm and $\Omega_2 = 0.01\gamma$, whereas x and y coordinates are scaled in millimeters. The other parameters are the same as Fig. 2. We set $p_2 = 0$ in Fig. 3(a) for the probe beam Ω_2. The topological charge is subsequently varied between -2 and 2. This represents a relatively simple case in which the intensity and phase profiles just display a single vortex case. As expected, no vortex is seen when $l_2 = 0$ confirming a Gaussian-shaped wave front of the laser field with a normal phase, whereas a doughnut appears in the intensity distribution with a dark (blue) hollow center for the nonzero l_2 [see Fig. 3(a)]. When $l_2 = 2$ or $l_2 = -2$, the generated beam has a relatively large hole, indicating a higher OAM index. In the phase profile, the number of 2π cycles around the circumference reads the OAM

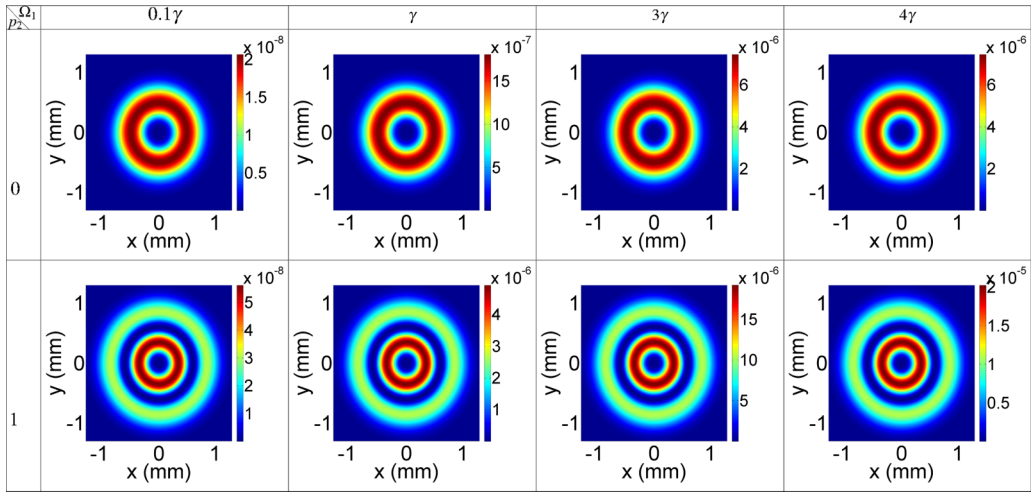

FIG. 4. The intensity profile of the FWM-generated field as a function of x and y for different values of strong cw field $\Omega_1 = 0.1\gamma,\ \gamma,\ 3\gamma$, and 4γ with $l_2 = 2,\ z = L$, and $p_2 = 0, 1$. Other parameters are the same as in Fig. 2.

number l_2. The helical phase patterns rotate inversely as the topological charge l_2 changes in sign. Results show a conserved exchange of optical vortices between applied and generated beams via the FWM process. Although the central zero-intensity hole always exists, the intensity profile of a vortex beam changes remarkably when taking into account the radial index p. Figure 3(b) exhibits the intensity and phase profiles for a nonzero radial index. The peak intensity of the FWM-generated field increases for higher values of the topological charge. Moreover, as can be seen in each intensity profile diagram, there is a clear dark ring between two bright rings, showing a $p_2 = 1$ radial index. Yet, the outer bright ring is too dim to be seen. Therefore, the intensity profile does not provide an accurate way to determine radial indices of the LG beam. Helical phase profiles, instead, allows to check different azimuthal and radial indices. Let us consider the case with l_2 and $p_2 = 1$, shown in the last diagram in the second row of Fig. 3(b). From the center to the border of the diagram, the phase profile sees two distinct zones. Apart from the center in which the phase is undefined and in both inner and outer zones, the phase diagram experiences $2\times 2\pi = 4\pi$, reading an azimuthal index of l_2. At the boundary of two zones, the phase undergoes a π shift, where the corresponding light goes to zero in intensity. Therefore, one can read a $p_2 = 1$ radial index for the generated beam.

Figure 4 illustrates the intensity profile of the FWM-generated field as a function of the azimuthal coordinates for different values of strong cw field $\Omega_1 = 0.1\gamma,\ \gamma,\ 3\gamma$, and 4γ with $l_2 = 2,\ z = L$, and $p_2 = 0, 1$. The other parameters are the same as in Fig. 2. Although a single ring appears

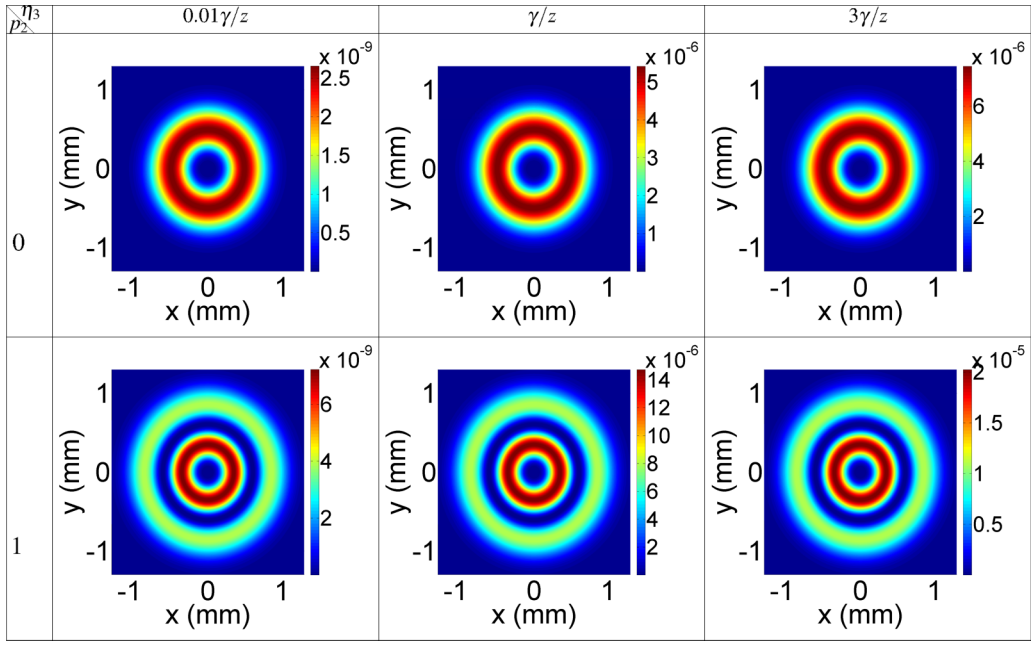

FIG. 5. The intensity profile of the FWM-generated field as a function of x and y for the different values of η_3, i.e., $0.01\gamma/z,\ \gamma/z$, and $3\gamma/z$ and $p_2 = 0, 1$ with $l_2 = 2$ and $z = L$. Other parameters are the same as in Fig. 2.

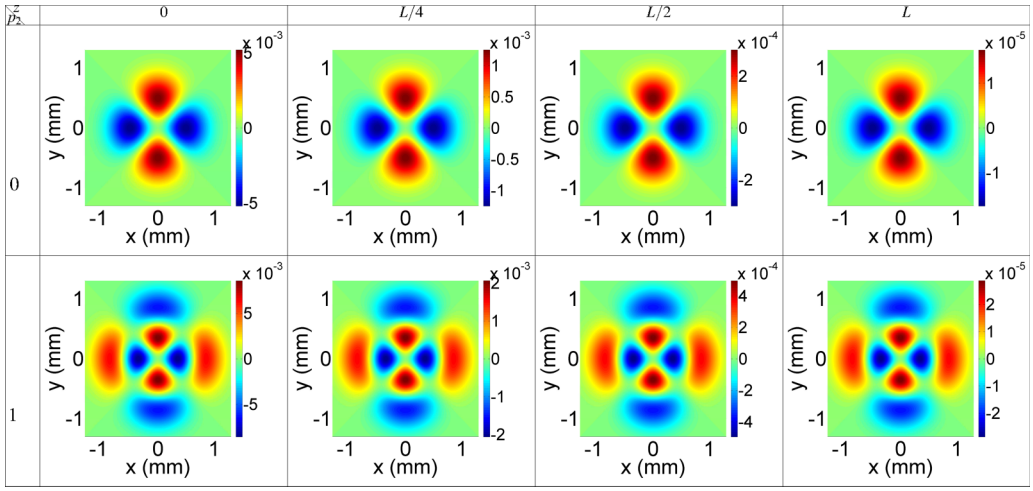

FIG. 6. The imaginary part of ρ_{30} profile as a function of x and y for different longitudinal distances $z = 0,\ L/4,\ L/2$, and L when $l_2 = 2$ and $p_2 = 0, 1$. Other parameters are the same as in Fig. 2.

for $p_2 = 0$ in the FWM-generated field intensity profile, two concentric rings emerge when $p = 1$ (see the second row of Fig. 4). Increasing the Rabi frequency of cw field Ω_1 enhances the FWM-generated field intensity, providing a more effective OAM exchange. In Fig. 5, we depict the intensity profile of the FWM-generated field as a function of x and y for the different values of η_3, i.e., $0.01\gamma/z,\ \gamma/z$, and $3\gamma/z$, and $p_2 = 0, 1$ with $l_2 = 2$ and $z = L$. The other parameters are the same as in Fig. 2. Both azimuthal and radial indices of applied beams remain constant over the OAM exchange process. The intensity of the FWM-generated field increases by increasing the η_3, indicating that the effective OAM transfer occurs for the larger values of η_3. Results presented in Figs. 4 and 5 imply that one can manipulate the efficiency of vortex conversion via Ω_1 and η_3.

We show in Fig. 6 the imaginary part of ρ_{30} as a function of x and y for different longitudinal distances $z = 0,\ L/4,\ L/2$, and L when $l_2 = 2$ and $p_2 = 0, 1$. The spatially dependent absorption profiles in the first row show the petal-like patterns with $2l_2$ number of petals when $p_2 = 0$. Introducing the radial index $p_2 = 1$ duplicates the number of petals. Although the absorption effects are dominant at the beginning of the sample, they reduce significantly on propagation. Note that the molecular magnets may experience a different nonzero detuning of applied fields in the presence of the various band effects. Fortunately, the EIT window in the SMM is established in a wide range of the detuning. As the exchange of OAM in a crystal of molecular magnets happens in the EIT window, the small band effect cannot effectively affect the results of OAM transfer in SMMs. Substituting Eqs. (10) and (11) into the imaginary part of ρ_{30}, one observes that $\mathrm{Im}[\rho_{30}]$ becomes very negligible for long-distances z, providing a lossless propagation of both fields which is in good agreement with the plots presented in Fig. 2.

B. Composite vortices

In what follows, we study a case where both vortex beams $\Omega_2(z = 0) = \Omega_2(r, \varphi)$ and $\Omega_3(z = 0) = \Omega_3(r, \varphi)$ are initially shining. Solving Eq. (11) for new boundary conditions, the propagation equation for the beam Ω_3 follows then

$$\Omega_3(r, \varphi, z) = \frac{\eta_3\Omega_2(r, \varphi)\Omega_4\Omega_1^* + \eta_2\Omega_3(r, \varphi)|\Omega_4|^2 + \eta_3 \exp\left(\frac{2z/L(-\eta_3|\Omega_1|^2-\eta_2|\Omega_4|^2)}{\gamma_3|\Omega_1|^2+\gamma_2|\Omega_4|^2)}\right)[\Omega_3(r, \varphi)|\Omega_1|^2 - \Omega_2(r, \varphi)\Omega_4\Omega_1^*]}{\eta_3|\Omega_1|^2 + \eta_2|\Omega_4|^2}. \quad (14)$$

According to Eq. (14), a new vortex beam (composite) is formed by collinear superposition of two initial vortices Ω_{2_0} and Ω_{3_0}, its characteristics may alter upon propagation by different factors. The intensity and helical phase profiles of the FWM-generated field Ω_3 are displayed in Figs. 7 and 8, respectively, for $\eta_2 = 0.9\eta_3,\ \eta_3 = 0.01\gamma/z, \gamma/z$, and $3\gamma/z$. Different modes of the probe LG fields are considered, i.e., $(l_2 = 1,\ l_3 = 2)$, $(l_2 = 1,\ l_3 = 3)$, $(l_2 = 1,\ l_3 = 4)$, and $(l_2 = 1,\ l_3 = 5)$ with $p_2 = 1,\ p_3 = 2$. We take $\Omega_{3_0} = 0.01\gamma$ and the other parameters are the same as in Fig. 3. The intensity and helical phase patterns of the FWM-generated field show a strong dependence on coupling parameters η_2 and η_3. It is clear from the left column of Fig. 7 that for $\eta_3 = 0.01\gamma/z$, the intensity distribution of the FWM-generated field has a multiple-ring shape, similar to the input field Ω_{3_0} with $p_2 = 2$. This indicates that the light-matter interaction is weak when $\eta_3 = 0.01\gamma/z$. The intensity distribution of the FWM-generated field is distorted for $\eta_3 = \gamma/z$ as the light-matter interaction becomes stronger by increasing η_3. More singularities emerge at the transverse plane associated with zero-intensity regions (the middle column). The position of peripheral vortices is shifted far away from the optical axis by increasing the value of η_3 from γ/z to $3\gamma/z$ (see the right column in this figure).

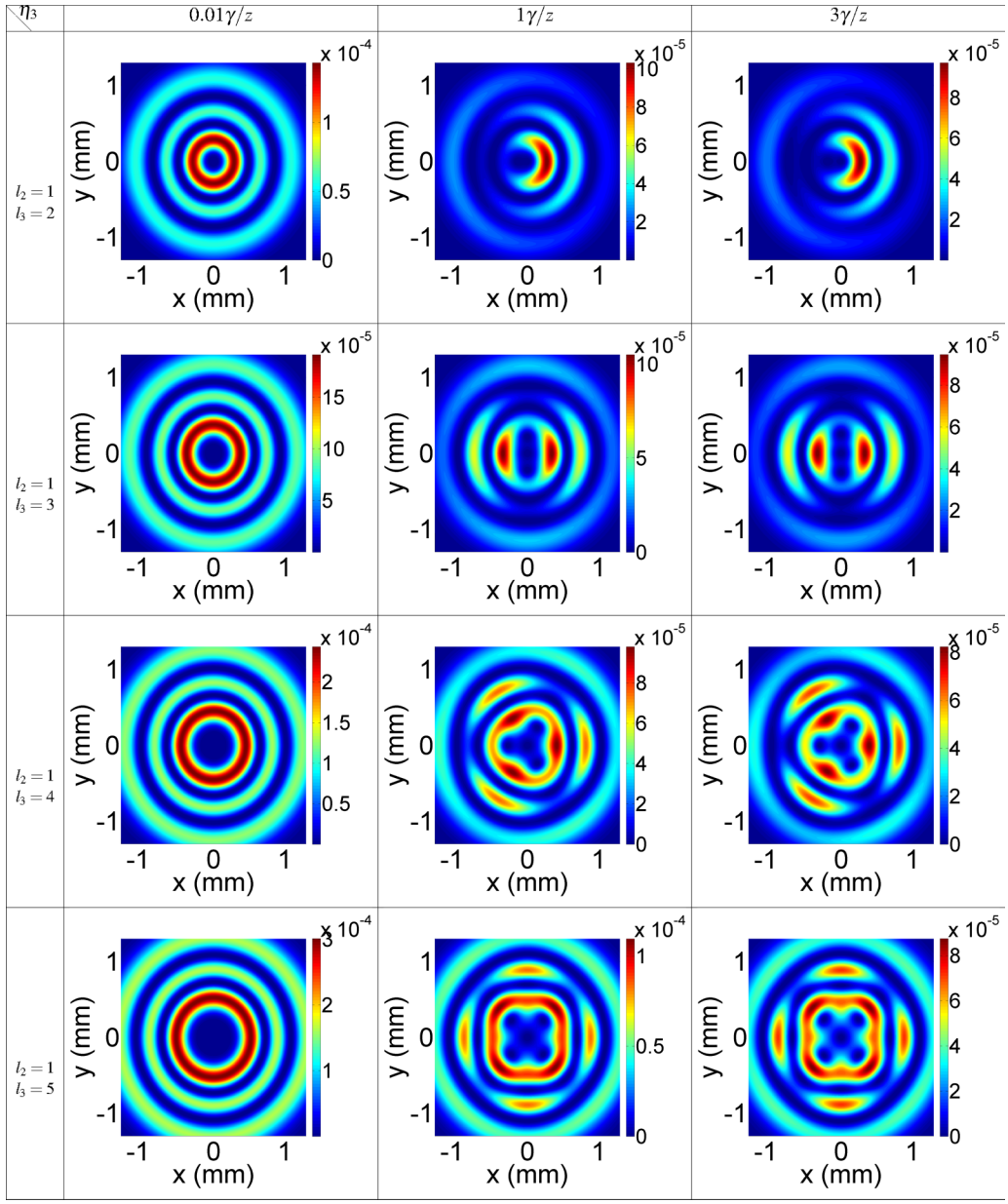

FIG. 7. The intensity profiles of the FWM-generated field versus x and y for the different modes of the weak probe LG fields, i.e., ($l_2 = 1$, $l_3 = 2$), ($l_2 = 1$, $l_3 = 3$), ($l_2 = 1$, $l_3 = 4$) and ($l_2 = 1$, $l_3 = 5$) with $p_2 = 1$, $p_3 = 2$ for $\eta_3 = 0.01\gamma/z$, γ/z, and $3\gamma/z$ in $z = L$. We take $\Omega_{3_0} = 0.01\gamma$, and the other parameters are the same as in Fig. 3.

The patterns illustrated in Fig. 8 exhibit the number of singularities in the phase of resulting light. Generally, the composite beam acquires a vortex of vorticity $|l_2|$ located at the beam core which is surrounded by $|l_2 - l_3|$ peripheral vortices. The normalized fidelity F describes how faithfully the FWM-generated $\Omega_3(r, \varphi, z)$ is created ($0 \leqslant F \leqslant 1$) [64]. It can be calculated from the overlap integral of the FWM-generated field $\Omega_3(r, \varphi, z)$ generated by the incident FWM field $\Omega_3(r, \varphi, z = 0)$,

$$F = \left| \frac{\int_x \int_y \Omega_3(x, y, z)\Omega_3^*(x, y, z = 0)dx\,dy}{N_f} \right|^2, \qquad (15)$$

where $N_f = (\int_x \int_y |\Omega_3(x, y, z=0)|^2 dx\,dy)^{1/2} (\int_x \int_y |\Omega_3(x, y, z)|^2 dx\,dy)^{1/2}$ is the normalization constant. In order to measure the quality of the FWM-generated field $\Omega_3(r, \varphi, z)$ in comparison with the incident probe field $\Omega_3(r, \varphi, z = 0)$, we investigate the normalized fidelity F versus the dimensionless distance z/L for azimuthal indices $l_3 = 2$, $l_3 = 3$, $l_3 = 4$ with (a) $p_2 = 1$, $p_3 = 2$, $l_2 = 1$ and different radial indices $p_3 = 0$, $p_3 = 1$, and $p_3 = 2$ with (b) $l_2 = 1$, $l_3 = 4$, and $p_2 = 1$ of the FWM-generated field in Fig. 9. The other parameters are the same as in Fig. 7. It is demonstrated that the normalized fidelity depends on azimuthal and radial indices as propagating inside the SMMs crystal. The fidelity changes from 0.3 to about 0.86 at the output plane of the crystal,

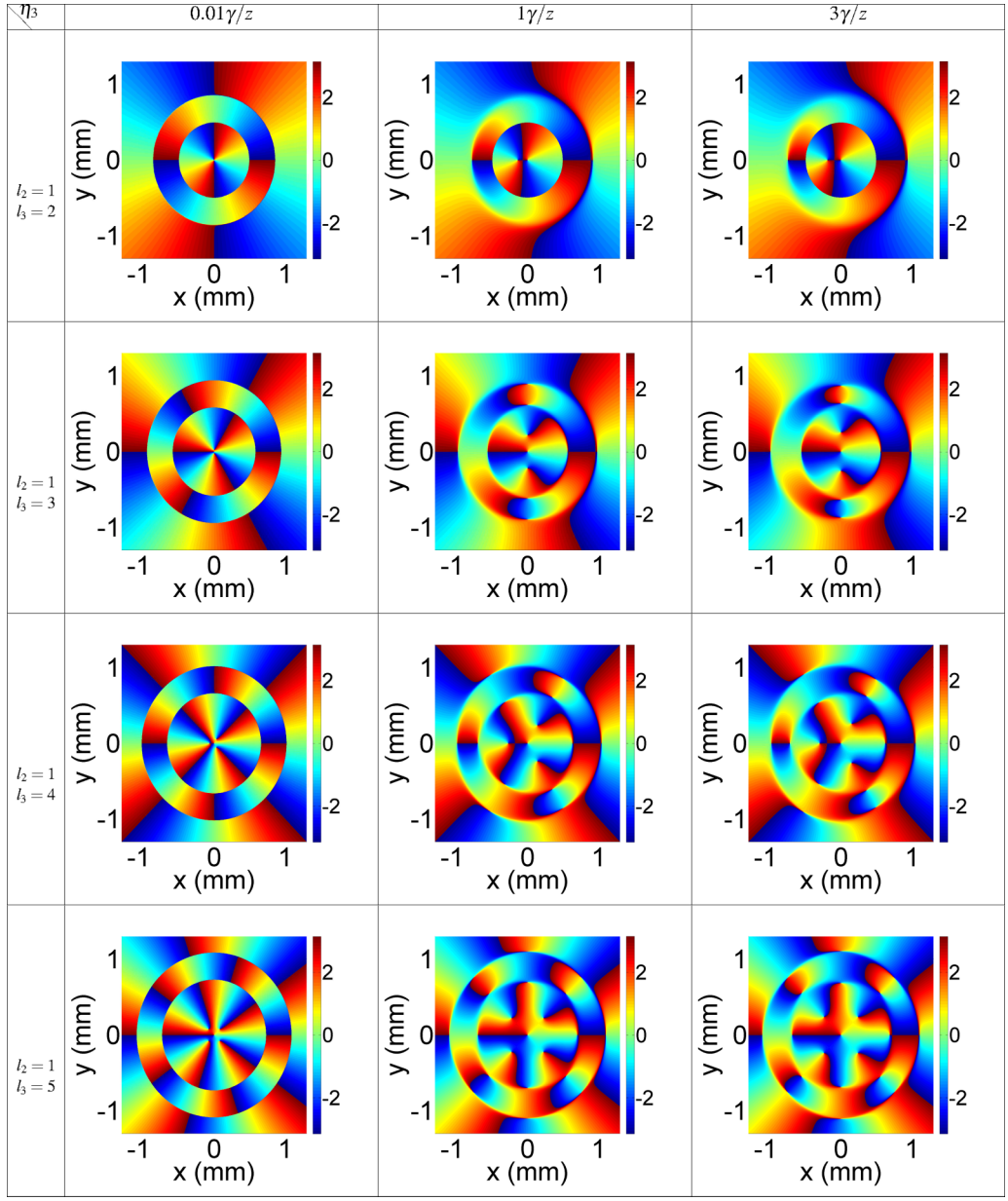

FIG. 8. The phase profiles of the FWM-generated field versus x and y. The parameters used here are the same as Fig. 7.

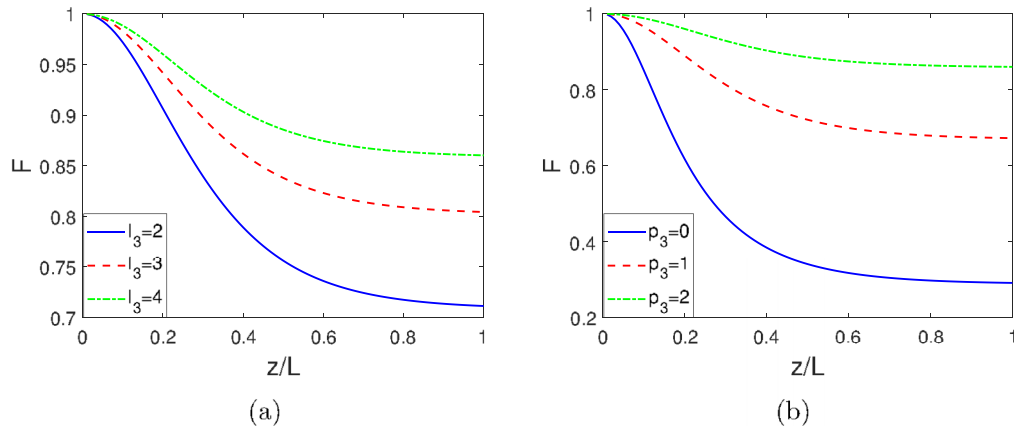

FIG. 9. The fidelity F versus the dimensionless distance z/L for different azimuthal indices $l_3 = 2$, $l_3 = 3$, $l_3 = 4$ with (a) $p_2 = 1$, $p_3 = 2$, $l_2 = 1$ and different radial indices $p_3 = 0$, $p_3 = 1$, and $p_3 = 2$ with (b) $p_2 = 1$, $l_2 = 1$, $l_3 = 4$. Other parameters are the same as in Fig. 7.

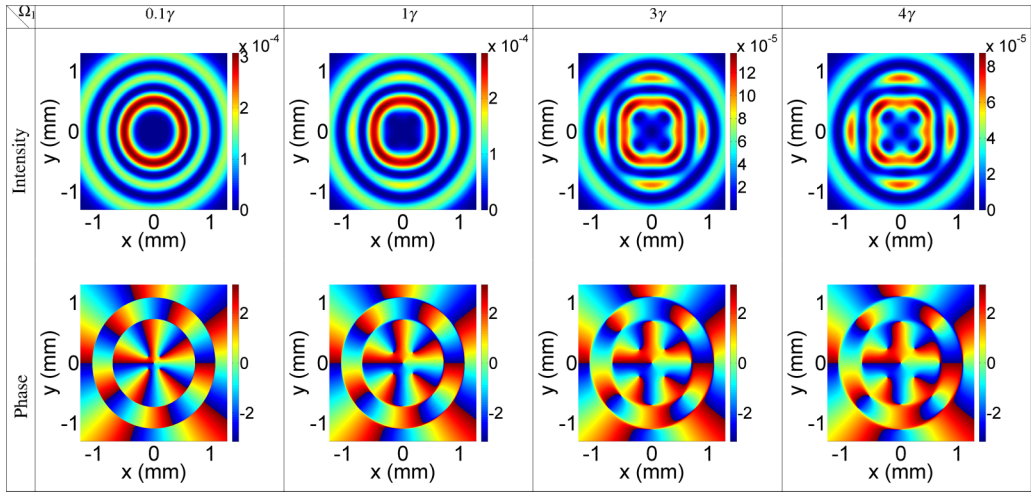

FIG. 10. The intensity and phase distribution the FWM-generated field as a function of x and y for $\Omega_1 = 0.1\gamma, \gamma, 3\gamma, 4\gamma$ with $l_2 = 1$, $p_2 = 1$, $l_3 = 5$, $p_3 = 2$, $\Omega_{2_0} = 0.01\gamma$, $\Omega_{3_0} = 0.01\gamma$, $z = L$. Other parameters are the same as in Fig. 2.

indicating the important role of radial indices on the quality of generation of the off-axis beam.

Figure 10 illustrates the effect of the strength of the strong cw field Ω_1 on the intensity distribution and the corresponding helical phase patterns. We consider $l_2 = 1$, $p_2 = 1$, $l_3 = 5$, $p_3 = 2$, $\eta_3 = 3\gamma/z$, and $\eta_2 = 0.9\eta_3$ in all plots of Fig. 10. It is shown that increasing the magnitude of Ω_1 results in asymmetric intensity profiles, whereas new off-axis vortices take place at the transverse plane. The obtained results in Figs. 7 and 10 illustrate that the parameters η_3, η_2, and Ω_1 affect the modulation of the FWM-generated off-axis beam behavior by controlling the strength of the light-matter coupling.

IV. CONCLUDING REMARKS

We have studied the interaction of optical vortices with a crystal of four-level molecular magnets. It has been shown that the OAM transfer between different frequencies can occur via the FWM mechanism in the microwave region. A weak probe vortex beam was considered to shine at the entrance to the sample. As a result of the FWM, an additional field is generated in the microwave domain with the same vorticity as that of the incident beam. By assuming two initially illuminating probe beams as optical vortices, the new vortices are generated with shifted axes propagating inside the medium. The position of the off-axis vortices can be controlled by the coupling parameters of the molecular magnets crystal and the strength of the strong cw electromagnetic fields. Calculating the normalized fidelity of the generated field, we have shown that the quality of the FWM depends strongly on the azimuthal and radial indices. Our proposed scheme may find potential application in the OAM exchange devices for quantum information processing.

ACKNOWLEDGMENTS

We would like to express the deepest appreciation to Professor G. Juzeliūnas for a useful discussion. Z.A.S. acknowledges financial support from Iran's National Elites Foundation (INEF) (Shahid Chamran's Scientific Prize, Grant No. 15/10597).

[1] D. Gatteschi, R. Sessoli, and J. Villain, *Molecular Nanomagnets* (Oxford University Press, New York, 2007).
[2] W. Wernsdorfer and R. Sessoli, Science **284**, 133 (1999).
[3] E. M. Chudnovsky and D. A. Garanin, Phys. Rev. Lett. **89**, 157201 (2002).
[4] J. R. Friedman, M. P. Sarachik, J. Tejada, and R. Ziolo, Phys. Rev. Lett. **76**, 3830 (1996).
[5] M. G. Benedict, P. Földi, and F. M. Peeters, Phys. Rev. B **72**, 214430 (2005).
[6] M. N. Leuenberger and D. Loss, Nature (London) **410**, 789 (2001).
[7] A. Ardavan, O. Rival, J. J. L. Morton, S. J. Blundell, A. M. Tyryshkin, G. A. Timco, and R. E. P. Winpenny, Phys. Rev. Lett. **98**, 057201 (2007).
[8] C. Timm and F. Elste, Phys. Rev. B **73**, 235304 (2006).
[9] A. V. Shvetsov, G. A. Vugalter, and A. I. Grebeneva, Phys. Rev. B **74**, 054416 (2006).
[10] Y. Wu and X. Yang, Phys. Rev. B **76**, 054425 (2007).
[11] Y. Wu and X. Yang, Appl. Phys. Lett. **91**, 094104 (2007).
[12] X. T. Xie, W. Li, J. Li, W. X. Yang, A. Yuan, and X. Yang, Phys. Rev. B **75**, 184423 (2007).
[13] I. D. Tokman, G. A. Vugalter, and A. I. Grebeneva, Phys. Rev. B **71**, 094431 (2005).
[14] L. Allen, M. W. Beijersbergen, R. J. C. Spreeuw, and J. P. Woerdman, Phys. Rev. A **45**, 8185 (1992).
[15] J. Wang, J. Y. Yang, I. M. Fazal, N. Ahmed, Y. Yan, H. Huang, Y. Ren, Y. Yue, S. Dolinar, M. Tur, and A. E. Willner, Nat. Photon. **6**, 488 (2012).
[16] N. Bozinovic, Y. Yue, Y. Ren, M. Tur, P. Kristensen, H. Huang, A. E. Willner, and S. Ramachandran, Science **340**, 1545 (2013).
[17] M. Padgett and R. Bowman, Nat. Photon. **5**, 343 (2011).
[18] G. Molina-Terriza, J. P. Torres, and L. Torner, Nat. Phys. **3**, 305 (2007).

[19] K. Liu, Y. Cheng, Z. Yang, H. Wang, Y. Qin, and X. Li, IEEE Anten. Wirel. Propag. Lett. **14**, 711 (2014).

[20] T. Yang, S. Li, O. Xu, W. Li, and Y. Wang, Remote Sens. Lett. **9**, 343 (2018).

[21] M. Lin, Y. Gao, P. Liu, and J. Liu, Int. J. Anten. Propag. **2016**, 1852659 (2016).

[22] H. Kawaguchi and H. Nakamura, IEEE Microw. Wirel. Compon. Lett. **29**, 504 (2019).

[23] F. Tamburini, E. Mari, A. Sponselli, B. Thidé, A. Bianchini, and F. Romanato, New J. Phys. **14**, 033001 (2012).

[24] X. Hui, S. Zheng, Y. Hu, C. Xu, X. Jin, H. Chi, and X. Zhang, IEEE Anten. Wirel. Propag. Lett. **14**, 966 (2015).

[25] Z. Zhang, S. Zheng, X. Jin, H. Chi, and X. Zhang, IEEE Anten. Wirel. Propag. Lett. **16**, 8 (2016).

[26] J. Ren and K. W. Leung, Appl. Phys. Lett. **112**, 131103 (2018).

[27] Y. Chen, S. Zheng, H. Chi, X. Jin, and X. Zhang, Electron. Lett. **52**, 684 (2016).

[28] Y. Chen, S. Zheng, Y. Li, X. Hui, X. Jin, H. Chi, and X. Zhang, IEEE Anten. Wirel. Propag. Lett. **15**, 1156 (2015).

[29] H. F. Huang and S. N. Li, IEEE Anten. Wirel. Propag. Lett. **18**, 432 (2019).

[30] M. Harris, C. A. Hill, P. R. Tapster, and J. M. Vaughan, Phys. Rev. A **49**, 3119 (1994).

[31] A. Mourka, J. Baumgartl, C. Shanor, K. Dholakia, and E. M. Wright, Opt. Express **19**, 5760 (2011).

[32] G. C. G. Berkhout and M. W. Beijersbergen, Phys. Rev. Lett. **101**, 100801 (2008).

[33] H. I. Sztul and R. R. Alfano, Opt. Lett. **31**, 999 (2006).

[34] J. Zhu, P. Zhang, Q. Li, F. Wang, C. Wang, Y. Zhou, J. Wang, H. Gao, L. C. Kwek, and F. Li, Sci. Rep. **9**, 7993 (2019).

[35] K. Dholakia, N. B. Simpson, M. J. Padgett, and L. Allen, Phys. Rev. A **54**, 3742(R) (1996).

[36] J. Courtial, K. Dholakia, L. Allen, and M. J. Padgett, Phys. Rev. A **56**, 4193 (1997).

[37] S. Barreiro, J. W. R. Tabosa, J. P. Torres, Y. Deyanova, and L. Torner, Opt. Lett. **29**, 1515 (2004).

[38] G. Walker, A. S. Arnold, and S. Franke-Arnold, Phys. Rev. Lett. **108**, 243601 (2012).

[39] D. Persuy, M. Ziegler, O. Crégut, K. Kheng, M. Gallart, B. Hönerlage, and P. Gilliot, Phys. Rev. B **92**, 115312 (2015).

[40] R. N. Lanning, Z. Xiao, M. Zhang, I. Novikova, E. E. Mikhailov, and J. P. Dowling, Phys. Rev. A **96**, 013830 (2017).

[41] Y. Li, Z. Y. Zhou, D. S. Ding, and B. S. Shi, J. Opt. Soc. Am. B **32**, 407 (2015).

[42] N. Radwell, T. W. Clark, B. Piccirillo, S. M. Barnett, and S. Franke-Arnold, Phys. Rev. Lett. **114**, 123603 (2015).

[43] H. R. Hamedi, V. Kudriašov, J. Ruseckas, and G. Juzeliunas, Opt. Express **26**, 28249 (2018).

[44] H. R. Hamedi, J. Ruseckas, E. Paspalakis, and G. Juzeliunas, Phys. Rev. A **101**, 063828 (2020).

[45] Y. Hong, Z. Wang, D. Ding, and B. Yu, Opt. Express **27**, 29863 (2019).

[46] J. Qiu, Z. Wang, D. Ding, W. Li, and B. Yu, Opt. Express **28**, 2975 (2020).

[47] D. Bortman-Arbiv, A. D. Wilson-Gordon, and H. Friedmann, Phys. Rev. A **63**, 031801(R) (2001).

[48] Z. Amini Sabegh, M. A. Maleki, and M. Mahmoudi, Sci. Rep. **9**, 3519 (2019).

[49] Z. Amini Sabegh, M. Mohammadi, M. A. Maleki, and M. Mahmoudi, J. Opt. Soc. Am. B **36**, 2757 (2019).

[50] J. Ruseckas, A. Mekys, and G. Juzeliunas, Phys. Rev. A **83**, 023812 (2011).

[51] J. Ruseckas, V. Kudriašov, I. A. Yu, and G. Juzeliunas, Phys. Rev. A **87**, 053840 (2013).

[52] H. R. Hamedi, J. Ruseckas, and G. Juzeliunas, Phys. Rev. A **98**, 013840 (2018).

[53] H. R. Hamedi, E. Paspalakis, G. Žlabys, G. Juzeliunas, and J. Ruseckas, Phys. Rev. A **100**, 023811 (2019).

[54] H. R. Hamedi, J. Ruseckas, E. Paspalakis, and G. Juzeliunas, Phys. Rev. A **99**, 033812 (2019).

[55] M. Mahdavi, Z. Amini Sabegh, M. Mohammadi, M. Mahmoudi, and H. R. Hamedi, Phys. Rev. A **101**, 063811 (2020).

[56] R. Sessoli, D. Gatteschi, A. Caneschi, and M. A. Novak, Nature (London) **365**, 141 (1993).

[57] A. L. Barra, D. Gatteschi, and R. Sessoli, Phys. Rev. B **56**, 8192 (1997).

[58] D. Dutta, G. Lefkidis, and W. Hübner, Phys. Scr. **95**, 065805 (2020).

[59] G. Lefkidis, C. Li, G. Pal, M. Blug, H. Kelm, H.-J. Krüge, and W. Hübner, J. Phys. Chem. A **115**, 1774 (2011).

[60] G. Lefkidis and W. Hübner, Phys. Rev. B **87**, 014404 (2013).

[61] B. W. Shore, K. Bergmann, A. Kuhn, S. Schiemann, J. Oreg, and J. H. Eberly, Phys. Rev. A **45**, 5297 (1992).

[62] M. O. Scully and M. S. Zubiary, *Quantum Optics* (Cambridge University Press, Cambridge, UK, 1997).

[63] L. Allen, M. J. Padgett, and M. Babiker, Prog. Opt. **39**, 291 (1999).

[64] R. Liu, F. Li, M. J. Padgett, and D. B. Phillips, Optica **2**, 1028 (2015).